Identification and characterization of an injury-induced skeletal progenitor

Owen Marecic[a,b,1], Ruth Tevlin[a,b,1], Adrian McArdle[a,b,1], Eun Young Seo[a,b], Taylor Wearda[a,b], Christopher Duldulao[a], Graham G. Walmsley[a,b], Allison Nguyen[b], Irving L. Weissman[b,2,3], Charles K. F. Chan[b,2,3], and Michael T. Longaker[a,b,2,3]

[a]Hagey Laboratory for Pediatric Regenerative Medicine, Division of Plastic and Reconstructive Surgery, Department of Surgery, Stanford University School of Medicine, Stanford, CA 94305-5148; and [b]Institute for Stem Cell Biology and Regenerative Medicine, Stanford University School of Medicine, Stanford, CA 94305

Contributed by Irving L. Weissman, July 7, 2015 (sent for review February 19, 2015)

The postnatal skeleton undergoes growth, remodeling, and repair. We hypothesized that skeletal progenitor cells active during these disparate phases are genetically and phenotypically distinct. We identified a highly potent regenerative cell type that we term the fracture-induced bone, cartilage, stromal progenitor (*f*-BCSP) in the fracture callus of adult mice. The *f*-BCSP possesses significantly enhanced skeletogenic potential compared with BCSPs harvested from uninjured bone. It also recapitulates many gene expression patterns involved in perinatal skeletogenesis. Our results indicate that the skeletal progenitor population is functionally stratified, containing distinct subsets responsible for growth, regeneration, and repair. Furthermore, our findings suggest that injury-induced changes to the skeletal stem and progenitor microenvironments could activate these cells and enhance their regenerative potential.

osteogenesis | skeletal stem/progenitor cell | fracture healing | regeneration | injury activation

Stem and progenitor cells mediate homeostasis and regeneration in postnatal tissue (1–6), but how these cells contribute to tissue repair, specifically fracture healing, is not well understood. Alterations in tissue microenvironments are known to influence stem cell behavior. Injury, infection, and aging have been shown to induce lineage skewing of hematopoietic stem cell (HSC) progeny (7–9). It is now known that HSCs are a diverse population of cells, including HSCs with lineage biases (10), that could model heterogeneity in other tissue stem cells (1, 11–13). Thus, we propose that fracture activates a distinct subset of skeletal stem and progenitor cells that mediate tissue regeneration and repair. If so, it is conceivable that specific stem or progenitor cells contribute to postnatal regeneration and, thus, could be implicated in cases of skeletal degeneration, such as osteoporosis, osteopenia, and impaired fracture healing.

Previously, our laboratory identified a pure clonal progenitor of bone, cartilage, and hematopoietic niche stromal cells (BCSP) in the appendicular skeleton of mice. We defined the BCSP by the immunophenotype ($CD45^-TER119^-Tie2^-AlphaV^+Thy^-6C3^-CD105^+$) and showed that it forms bone, cartilage, and at least three subsets of stromal cells (14). We also observed that the BCSP forms bone via endochondral ossification. Thus, we used a relative stability model of long-bone fracture healing to investigate how the BCSP contributes to bone repair. Recent studies report that bone injury induces progenitor expansion (15, 16), but they do not consider how phenotypic or transcriptional changes within these populations affect tissue regeneration. Our investigative approach allows us to characterize these changes in a specific, highly purified skeletal progenitor population. These findings advance the understanding of postnatal skeletal regeneration and repair on a cellular and molecular level.

Results

BCSP Expansion Precedes Ossified Callus Formation. Transverse, middiaphyseal, femoral fractures were made in 8-wk-old, C57BL/6 male mice (Fig. 1*A*). Intramedullary fixation enabled relative stability to facilitate endochondral ossification (17). The callus index (CI), defined as the maximum diameter of callus divided by the diameter of adjacent diaphysis, measured callus formation over time (Fig. 1*B*) (18). CI peaked significantly at postfracture day 14 and marked maximal callus formation (Fig. 1*C*, $^{****}P < 0.0001$). To determine whether BCSP expansion accompanies callus growth, individual uninjured femora and dissected fracture calluses were analyzed separately. Femoral calluses were dissected at postfracture days 3, 7, 14, 21, and 28. BCSPs were isolated using mechanical and enzymatic tissue dissociation and were stained for fluorescence-activated cell sorting (FACS). FACS analysis showed a significant increase in BCSP frequency after fracture, which peaked at postfracture day 7 (D7) (Fig. 2 *A* and *B*, $^{****}P < 0.0001$).

Hindlimb Irradiation Reduces Fracture-Induced BCSP Expansion. Radiotherapy is an important modality for the treatment of many malignancies; however, it often induces significant osseous side effects (19). We hypothesized that bone dysfunction correlates with reduced BCSP frequency. After hindlimb irradiation with 800 rad 12 h before fracture, delayed callus formation and prolonged healing was observed in irradiated femora (Fig. 2*C*; day 14, $^*P < 0.05$; day 21, $^*P < 0.05$). Notably, BCSP expansion was reduced significantly in irradiated versus nonirradiated D7 calluses (Fig. 2*D*, $^{**}P < 0.01$). Both callus development and BCSP expansion remained impaired 3 mo postirradiation (Fig. 2*E*, $^{**}P < 0.01$). These results suggest that BCSPs are necessary for functional bone regeneration.

Significance

Here, we characterize the injury-induced activation of a specific, highly purified population of multipotent skeletal progenitor cells. These activated progenitors show increased cell frequency, increased viability, and enhanced osteogenic potential. They also possess a unique transcriptional profile that distinguishes them from progenitors found in uninjured bone. We report that these features improve regenerative capacity, suggesting that activated progenitors play a principal role in bone healing. We hope that a better understanding of stem and progenitor activation will inspire novel therapies that restore impaired skeletal regeneration.

Author contributions: O.M., R.T., A.M., E.Y.S., C.K.F.C., I.L.W., and M.T.L. designed research; O.M., R.T., A.M., E.Y.S., T.W., C.D., G.G.W., A.N., and C.K.F.C. performed research; O.M., R.T., A.M., E.Y.S., and C.K.F.C. analyzed data; O.M., R.T., A.M., E.Y.S., and C.K.F.C. wrote the paper; and I.L.W. and M.T.L. supervised the laboratory.

The authors declare no conflict of interest.

[1]O.M., R.T., and A.M. contributed equally to this work.

[2]C.K.F.C., I.L.W., and M.T.L. contributed equally to this work.

[3]To whom correspondence may be addressed. Email: chazchan@stanford.edu, irv@stanford.edu, or longaker@stanford.edu.

This article contains supporting information online at www.pnas.org/lookup/suppl/doi:10.1073/pnas.1513066112/-/DCSupplemental.

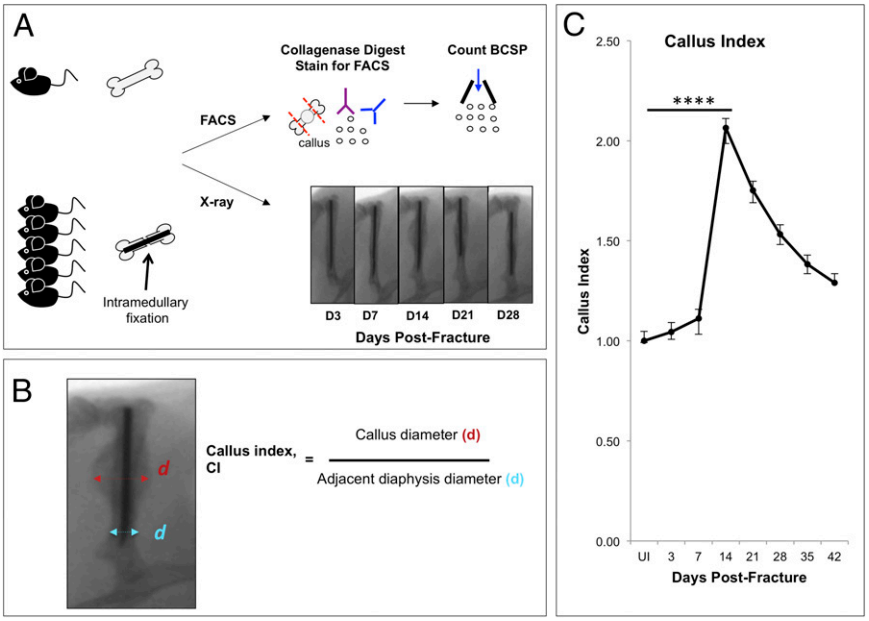

Fig. 1. BCSPs were isolated from mouse femora. (*A*) Schematic showing our experimental model, including fracture induction, tissue dissection (fracture calluses were dissected at postfracture days 3, 7, 14, 21, and 28), and BCSP isolation via FACS. (*B*) Callus index (CI) is a ratio of fracture callus diameter to adjacent diaphysis diameter (red, callus diameter; blue, diaphysis diameter). (*C*) CI peaks at postfracture day 14 (****$P < 0.0001$, $n = 9$ femora; D14 CI, 2.06 ± 0.08; Student's *t* test).

Injury Induces Phenotypic Changes in BCSPs. We next investigated injury-induced phenotypic changes in BCSPs. FACS-isolated BCSPs from uninjured femora (uninjured-BCSP, *u*-BCSP) and D7 fracture calluses (fracture-BCSP, *f*-BCSP) were pooled separately for in vitro and in vivo assays (Fig. 3*A*). *f*-BCSPs demonstrated significantly increased plating efficiency, as determined by colony number (Fig. 3*B*, *$P < 0.05$), significantly greater viability (Fig. 3*C*, *$P < 0.05$), and markedly reduced apoptotic activity

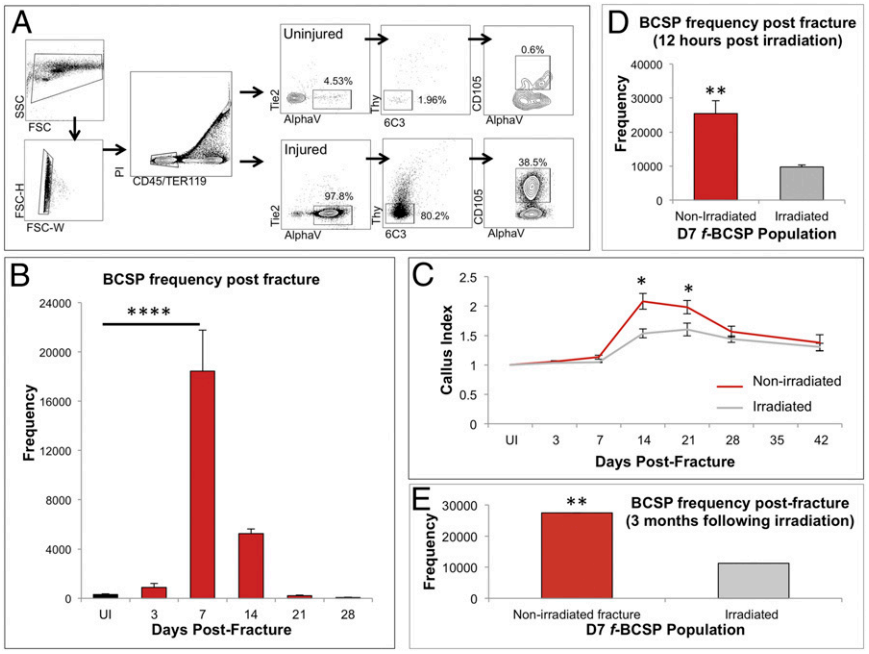

Fig. 2. BCSP expansion precedes callus formation. (*A*) FACS analysis shows BCSP expansion after fracture. (*B*) Bar graph showing a significant increase in the frequency of BCSPs at postfracture day 7 versus uninjured (UI) control (****$P < 0.0001$; UI, 307 ± 61, $n = 8$; D7, 18,444 ± 3,314, $n = 9$; Student's *t* test). Data represent mean cell frequencies of individual samples. Whole UI femora were used whereas calluses were dissected. (*C*) CI is significantly reduced in irradiated calluses versus nonirradiated controls (*$P < 0.05$, $n = 4$–6, Student's *t* test). (*D*) Bar graph showing a significant reduction in the frequency of BCSPs at postfracture day 7 (D7 *f*-BCSP) in irradiated calluses versus nonirradiated controls (**$P < 0.01$, $n = 5$ calluses; nonirradiated, 25,442 ± 3,758; irradiated, 9,739 ± 562; Student's *t* test). (*E*) Bar graph showing D7 *f*-BCSP frequency remains depleted in irradiated calluses versus nonirradiated controls when fracture is induced 3 mo postirradiation (**$P < 0.01$, $n = 3$–5 calluses; nonirradiated, 27,478 ± 12; irradiated, 11,267 ± 6; Student's *t* test).

(Fig. 3*D*). Furthermore, in vitro immunofluorescence staining showed that *f*-BCSP–derived colonies form bone via a collagen II intermediate, as previously shown by the *u*-BCSP (1, 14) (Fig. 3*E*).

Osteogenic potential was examined in vitro and in vivo. Alkaline phosphatase activity, an intermediate marker of bone formation, and alizarin red stain, an extracellular matrix mineralization marker, were used to measure osteogenic potential in vitro. *f*-BCSPs showed significantly greater alkaline phosphatase activity and alizarin red stain relative to *u*-BCSPs (Fig. 4 *A* and *B*, alizarin quantification, $^{****}P < 0.0001$). A model of ectopic bone formation previously described by our laboratory was used to determine osteogenic activity in vivo (20). In short, 20,000 GFP-labeled, FACS-isolated cells from each BCSP population were transplanted separately under the renal capsules of immunodeficient mice (Fig. 3*A*). Grafts were explanted after 4 wk. Both populations formed ectopic bone and marrow (20), but engrafted *f*-BCSPs formed significantly larger bone specimens (Fig. 4*C*, *Top* and *Middle* and Fig. 4*D*, $^{*}P < 0.05$). These phenotypic differences could describe progenitor activation or characterize a more regenerative progenitor subpopulation.

Differential Gene Expression Characterizes BCSP Response to Injury. We investigated the transcriptional mechanisms underlying these phenotypic differences using microarray analysis. Representative genes involved in cell survival, osteogenesis, chondrogenesis, and angiogenesis were analyzed (Fig. 5*A*) using the Gene Expression Commons (*Materials and Methods*) (21). Analysis included BCSPs isolated from uninjured femora at postnatal days 3 (P3, *u*-BCSP) and 56 (P56, *u*-BCSP) and from calluses at postfracture days 3 (D3) and 7 (D7).

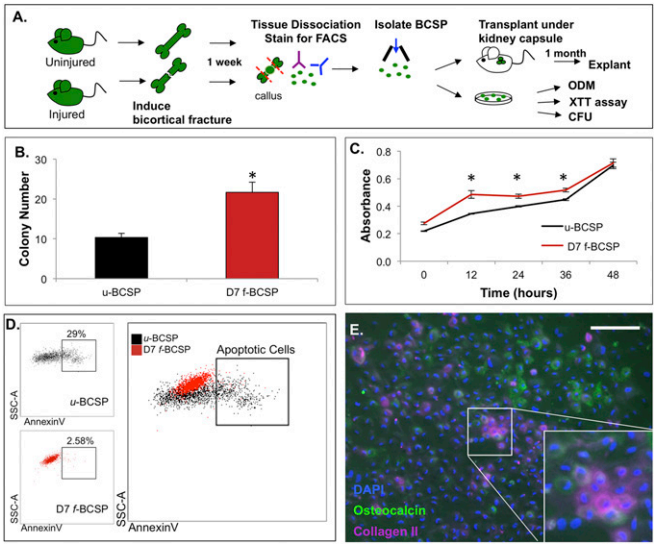

Fig. 3. Injury induces phenotypic changes in BCSPs. (*A*) Schematic showing experimental model for in vitro and in vivo assays (ODM, osteogenic differentiation media; XTT, viability assay; CFU, colony-forming units). (*B*) Bar graph showing D7 *f*-BCSPs form significantly more colonies than *u*-BCSP ($^{*}P < 0.05$, $n = 3$; *f*-BCSP, 22 ± 4.40; *u*-BCSP, 10.33 ± 1.88; Student's *t* test). (*C*) XTT cell viability curves show that D7 *f*-BCSPs are significantly more viable than adult *u*-BCSPs within 36 h of plating ($^{*}P < 0.05$, $n = 3$; Student's *t* test). (*D*) FACS analysis showing *u*-BCSPs (*Top Left*, black) have greater apoptotic activity than *f*-BCSPs (*Bottom Left*, red). The percentage of Annexin V-positive cells is listed in each plot on the *Left*. A merged plot of *u*-BCSPs (black) and *f*-BCSPs (red) is shown on the *Right*. (*E*) Immunofluorescence staining shows that *f*-BCSPs form bone (osteocalcin, green) through a cartilaginous intermediate (collagen II, purple) as seen previously in the *u*-BCSP (14). DAPI, blue. (Scale bar: 1 mm; Magnification, *Inset*: 2.5×.)

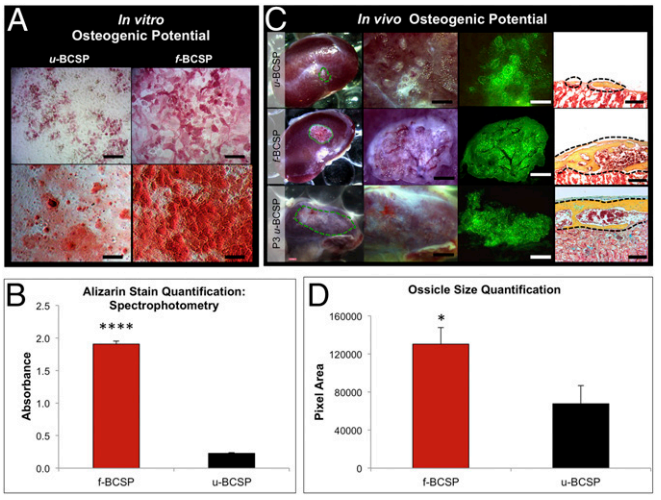

Fig. 4. *f*-BCSPs have enhanced osteogenic potential. (*A*) Staining for alkaline phosphatase activity (*Top*) and alizarin red (*Bottom*) shows enhanced osteogenic activity of *f*-BCSPs versus *u*-BCSPs in vitro. (Scale bars: 200 μm.) (*B*) Bar graph of alizarin red absorbance shows significantly greater staining in *f*-BCSPs versus *u*-BCSPs ($^{****}P < 0.0001$, $n = 3$; *f*-BCSP, 1.907 ± 0.046; *u*-BCSP, 0.228 ± 0.009; Student's *t* test). (*C*) GFP-labeled BCSPs transplanted under renal capsules show ectopic bone formation in vivo. *f*-BCSP grafts (*Middle*) are larger than those of adult *u*-BCSPs (*Top*). *f*-BCSP grafts more closely resemble perinatal *u*-BCSP (P3 *u*-BCSP) grafts in size (*Bottom*). (*Far Left*) Brightfield; (*Left*) brightfield. (Scale bars: 1 mm.) (*Right*) Fluorescent microscopy. (Scale bars: 1 mm.) (*Far Right*) Movat's Pentachrome stain of explanted tissue (yellow, bone; blue, cartilage; brown, marrow; red, renal tissue), brightfield. (Scale bars: 200 μm.) (*D*) Bar graph showing significantly greater in vivo ectopic bone formation by *f*-BCSPs versus *u*-BCSPs ($^{*}P < 0.05$; *f*-BCSP, 130,391.29 ± 17,444.52, $n = 7$; *u*-BCSP, 67,729.63 ± 19,077.15, $n = 8$; Student's *t* test).

Cell survival factor analysis showed differential apoptotic gene expression between groups (Fig. 5*A*, fifth cluster from top). Notably, D7 *f*-BCSPs down-regulated the following apoptotic factors: *B-cell leukemia/lymphoma 10*, *Caspase3*, *Dido1*, *Mitochondrial ubiquitin ligase activator 1*, and *Cell division cycle and apoptosis regulator 1* (22, 23). These data support reduced *f*-BCSP apoptotic activity seen in Fig. 3*D*.

Skeletogenic analysis showed that all groups maintain high expression levels of *Runx2* and *Sox9*, master regulator genes of skeletal growth and development (24, 25), and *BMP2*, a major postnatal bone-forming factor (26) (Fig. 5*A*, first cluster from top). Expression of osteogenic signaling pathway (*BMP2*; canonical Wnt) antagonists was down-regulated in D7 *f*-BCSP (Fig. 5*A*, second cluster from top). Down-regulated BMP antagonists include *Gremlin1* and *Chordin* (27, 28), and down-regulated Wnt antagonists include *Dikkopf1* (*Dkk1*), *Secreted frizzled-related protein* (Sfrp)-*4*, *Sfrp5*, and *Wnt inhibitory factor 1* (*Wif1*) (29–31).

Hedgehog pathway analysis showed that *Indian hedgehog* (*Ihh*) expression increases whereas *Parathyroid hormone-like peptide* (*Pthlh*) expression decreases in D7 *f*-BCSP (Fig. 5*A*, third cluster from top). *Parathyroid hormone receptor 1* expression remains high. In addition, *Ihh* pathway antagonist, *Hedgehog interacting protein* (*Hhip*), is down-regulated whereas *Dispatched-1* (*Disp1*), a protein involved in *Ihh* secretion, is up-regulated (32). Interestingly, expression of *Collagen 10α1* (*Col10α1*), a hypertrophic chondrocyte marker, is up-regulated as well (33). These data suggest that fracture activates hedgehog signaling in *f*-BCSPs.

Angiogenic factor analysis (Fig. 5*A*, fourth cluster from top) showed that the expression of *Vascular endothelial growth factor* alpha (*Vegfα*) is up-regulated in D7 *f*-BCSP and that *Placental growth factor* (*Plgf*), a member of the VEGF family (20), rises in D3 *f*-BCSP. Transcriptional expression of *Dicer1*, a factor required

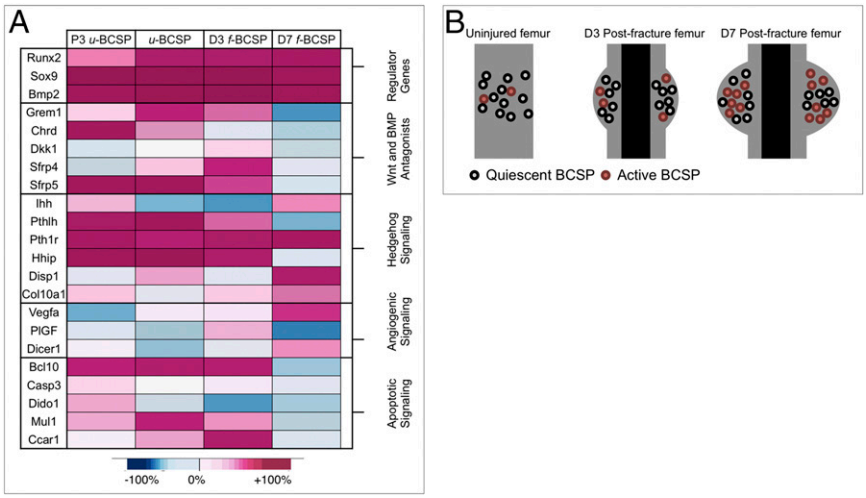

Fig. 5. BCSPs show differential gene expression during disparate phases of skeletal growth. (*A*) Heatmap showing differential gene expression between FACS-isolated BCSPs using microarray analysis. Genes representative of skeletogenesis (*Left*) are clustered according to function (*Right*). Scale: pink, high expression; blue, low expression. (*B*) Schematic showing that *u*-BCSPs predominate skeletal homeostasis (*Left*). Injury induces BCSP expansion at the injury site (*Middle*, postfracture day 3) to mediate healing (*Right*, postfracture day 7). Gray cell, *u*-BCSP; red cell, *f*-BCSP.

for murine embryonic angiogenesis (34), is up-regulated in D7 *f*-BCSP. Cumulatively, these data mechanistically support *f*-BCSP activation (Fig. 5*B*).

CD49f^{+} Expression Identifies Activated *f*-BCSP. Because *f*-BCSPs and P3 *u*-BCSPs (Fig. 4C, *Bottom Row*) formed more bone in vivo than *u*-BCSPs, we used microarray data to identify surface marker expression selective for *f*-BCSPs and P3 *u*-BCSPs. Integrin subunit α6 (defined by the *CD49f* surface marker) expression is up-regulated in both *f*-BCSPs and P3 *u*-BCSPs, but not in *u*-BCSPs (Fig. 6*A*). Expression of its beta-components, integrin subunit β1 and integrin subunit β4, remains low. Because *CD49f* expression diminishes gradually with age (Fig. S1), we hypothesized that it could classify a more regenerative *f*-BCSP subpopulation. Thus, phenotypic differences between *CD49f*$^{+/-}$ *f*-BCSPs were investigated. *CD49f*$^{+/-}$ *f*-BCSPs were isolated as previously described with an additional antibody for *CD49f*. FACS analysis showed that the proportion of *CD49f*$^{+}$ *f*-BCSPs increases relative to *CD49f*$^{-}$

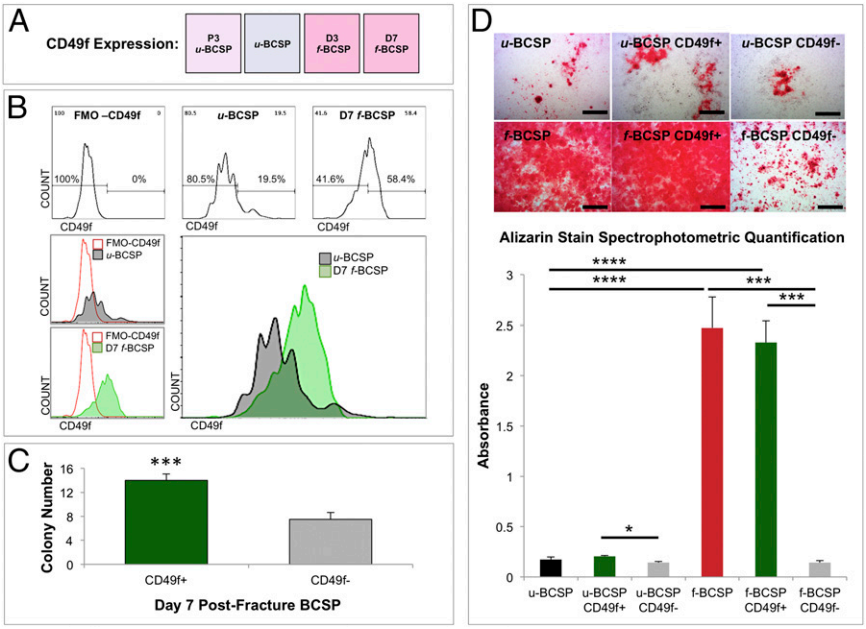

Fig. 6. *CD49f*$^{+}$ expression identifies activated *f*-BCSPs. (*A*) Microarray analysis of FACS-isolated BCSP populations shows that *CD49f* expression is recapitulated after injury. (*B*) FACS analysis showing *CD49f*$^{+}$ expression increases after fracture (merged FACS plot, *Bottom Right*). *CD49f* expression of D7 *f*-BCSPs (*Top Right*) was compared with *u*-BCSPs (*Top Middle*) and a negative control (FMO-CD49f, *Top Left*). (*C*) Bar graph showing *CD49f*$^{+}$ *f*-BCSPs form significantly more colonies than *CD49f*$^{-}$ *f*-BCSPs in vitro (***$P < 0.001$, $n = 9$; *CD49f*$^{+}$, 16 ± 1.32; *CD49f*$^{-}$ 8.5 ± 0.96; Student's *t* test). (*D*, *Top*) The osteogenic potential of FACS-isolated BCSP populations was assayed in vitro using alizarin red staining. (*Bottom*) Results were quantified using spectrophotometry to measure absorbance. *f*-BCSPs have significantly enhanced osteogenic potential compared with *u*-BCSPs (****$P < 0.0001$, $n = 3$; Student's *t* test), as shown previously. Further subfractionation of the *f*-BCSP population demonstrates that *CD49f*$^{+}$ *f*-BCSPs are significantly more osteogenic than *CD49f*$^{-}$ *f*-BCSPs (***$P < 0.001$, $n = 3$, Student's *t* test).

f-BCSPs after fracture (Fig. 6*B* and Fig. S2 *A* and *B*). In vitro assays demonstrate that *CD49f*$^+$ *f*-BCSPs form significantly more colonies (Fig. 6*C*, $^{***}P < 0.001$) and have significantly greater osteogenic potential than *CD49f*$^-$ *f*-BCSPs (Fig. 6*D*, $^{***}P < 0.001$ and Fig. S2 *C* and *D*). These data could identify *CD49f* as an activation marker, or they could demonstrate the selective expansion of a minor subpopulation of *CD49f*$^+$ cells in adult *u*-BCSP populations during bone repair.

Discussion

Our experiments show that injury-induced BCSP expansion precedes ossified callus formation shortly after injury, suggesting BCSP mediation of osseous healing. Recent work by Tabin and coworkers suggests that irradiation induces skeletal progenitor dysfunction that disrupts skeletal development (35). Here, we show that hindlimb irradiation before fracture suppresses *f*-BCSP expansion and delays callus formation. Thus, we propose that postnatal skeletal repair depends on a functional progenitor response at the fracture site.

We also describe injury-induced variations between BCSP phenotypes. Of particular note, the in vivo intrinsic bone-forming capacity of *f*-BCSPs resembles that of P3 *u*-BCSPs more closely than that of adult *u*-BCSPs. These findings suggest that *f*-BCSPs maintain perinatal phenotypes in the postnatal adult skeleton. This phenomenon could occur via the activation of all tissue-resident BCSPs or the expansion of specific BCSPs with greater regenerative capacity.

Phenotypic variations between BCSPs isolated during different periods of skeletal growth are supported by microarray data. Notably, whereas expression of skeletogenic factors remains high in all groups, *f*-BCSPs show significantly greater osteogenic capacity than *u*-BCSPs. Perhaps, differential gene expression, including the down-regulation of osteogenic pathway antagonists, the recapitulation of embryonic skeletogenic factors, and/or the mediation of tissue revascularization, augments the skeletogenic potential of *f*-BCSPs. Comprehensive transcriptional analyses of BCSP-mediated repair, although beyond the scope of our study, is amenable to future examination.

Of particular importance, however, is the differential expression of *CD49f*. We show that fracture results in local expansion of *CD49f*$^+$ BCSPs, as observed in the callus proper and to a lesser degree in noncallused tissue of the fractured femur. BCSP expansion is not seen in the contralateral uninjured femur (Fig. S2). *CD49f* expression enables the segregation of pure human HSCs from multipotent progenitors (36); however, our laboratory demonstrated that blocking its function in mouse HSC was inconsequential (37). Perhaps *CD49f* expression identifies a more regenerative BCSP subpopulation in the postnatal skeleton.

Our findings indicate that a specific skeletal progenitor (termed *f*-BCSP) plays a key role in postnatal skeletal repair in mice. The *f*-BCSP is distinct from progenitors isolated from uninjured bone and is characterized by *CD49f*$^+$. *CD49f*$^+$ *f*-BCSPs have enhanced regenerative potential and are active during acute periods of repair. A better understanding of the requisite stimuli for bone repair offers translational promise because cell-specific activation could enhance osteogenesis amid dysfunctional bone health.

Materials and Methods

Mice. C57BL/6, C57BL/6-β-actin-EGFP, C57BL6/Rag-2/γ(c)KO mouse strains were derived and maintained in our laboratory. Animals used in this experiment were 8-wk-old male mice. All animals were maintained in Stanford University Laboratory Animal Facilities in accordance with Institutional Animal Care and Use Committee and National Institutes of Health (NIH) guidelines. All procedures in this experiment were performed in accordance with Stanford Administrative Panel on Laboratory Animal Care Protocol 27757.

Mouse Femoral Fracture. Mice were anesthetized using inhalational isoflurane. Analgesia was given before medial parapatellar incision. The patella was dislocated laterally to expose femoral condyles. The medullary cavity was reamed with a 26.5G needle (BD) before insertion of an intramedullary pin of equal diameter. The femur was fractured at its midpoint using a scissors. The pin remained in situ to stabilize the fracture and allow for postoperative mobility. The patella was relocated, muscles were reapproximated, and the skin was closed using a 6/0 nylon suture.

X-Ray Assessment. Femoral fractures were followed using a SPECTRAL Ami X Optical Imaging Platform with a 40-kV variable energy X-ray source (Spectral Instruments Imaging, LLC). Mice were anesthetized using inhalational isoflurane and pronated on the scanning platform, with the fractured limb abducted and the knee joint aligned flat at 90°. A high-resolution digital image was acquired. Mice were scanned weekly for 7 wk.

Isolation of Skeletal Progenitor Cells. Complete, uninjured femora from uninjured mice and dissected fracture calluses from postfracture days 3, 7, 14, 21, and 28 were harvested. Each sample was crushed separately using mortar and pestle and placed in independent conicals with 10 mL of collagenase at room temperature. Each sample underwent three serial enzymatic digestions in collagenase with DNase at 37 °C for 30 min under gentle agitation. Dissociated cells were filtered through a 40-μm nylon mesh, pelleted at 200 × *g* at 4 °C, resuspended in staining media [2% (vol/vol) FBS in PBS], and layered onto a histopaque gradient before centrifugation at 500 × *g* for 15 min at room temperature with zero acceleration. The cloudy cellular interphase was pipetted off, washed with staining media, and centrifuged. The pellet was stained with fluorochrome-conjugated antibodies against CD45, Tie2, α_v-integrin, CD105, and Thy 1.1 for purification by flow cytometry (14). An additional stain for *CD49f* was included as needed. To determine cell frequency, each sample was analyzed separately. Samples were pooled for in vitro and in vivo experiments.

In Vitro Osteogenic Potential. FACS-isolated BCSPs were harvested from uninjured femora and postfracture day 7 calluses. Then, 10,000 cells were plated in triplicate and were maintained in MEMα, 20% FBS, and 1% Penstrep. Once 80% confluent, cells were transferred to osteogenic differentiation media (ODM) (38). Two stains were used. Alkaline phosphatase activity was measured after 7 d in ODM. Alizarin red staining was done after 14 d in ODM. Results were imaged at 5× magnification. To quantify the alizarin red stain, each well was washed briefly in PBS, followed by a 15-min wash in 20% methanol/10% acetic acid in ddH_2O under gentle agitation to lift the stain. Absorbance was measured via spectrophotometry at 450 nm.

Colony-Forming Units. Five hundred cells of each population were plated in triplicate and maintained in MEMα, 10% FBS, and 1% Penstrep for 2 wk before colony counting.

XTT Assay. A trypan blue exclusion assay was used to assess cell viability. Viable cells were counted using light microscopy. The [2,3-bis-(2-methoxy-4-nitro-5-sulfophenyl)-2*H*-tetrazolium-5-carboxanilide] (XTT) assay (Cell Proliferation Kit II XTT; Roche Applied Science) was done per the manufacturer's instructions. Briefly, 1,000 cells of each population were plated in triplicate and maintained in culture medium. Proliferation was evaluated every 12 h. The absorbance of each well was determined using a microplate reader at 492 nm and 690 nm (SpectraMAX 384 Plus; Molecular Devices Ltd.).

Transplantation of Skeletal Progenitor Subsets and Analysis of Kidney Grafts. FACS-isolated BCSPs were pelleted and resuspended in 2 μL of Growth Factor Reduced Matrigel (BD Biosciences). Each population was transplanted beneath independent kidney capsule of anesthetized age- and sex-matched immunocompromised mice. Engrafted kidneys were harvested and imaged after 4 wk. Kidneys were fixed in 2% paraformaldehyde overnight at 4 °C, decalcified for 2 wk at 4 °C using 19% EDTA solution, and embedded in optimal cutting temperature for cryosectioning. Representative sections were stained with Movat's Pentachrome stain (39). To quantify kidney grafts, analytical software (Adobe Photoshop CS6) was used to measure pixel area of engrafted bone specimens. Images are 35× magnification.

Microarray Analyses of Bone Marrow Stromal Progenitors. Microarray analyses were done on highly purified, double-sorted cell populations. Each population was sorted into TRIzol (Life Technologies) in three independent sorts. RNA was isolated with RNeasy Micro Kit (Qiagen) per the manufacturer's instructions. RNA was amplified twice with a RiboAmp RNA amplification kit (Arcturus Engineering). Amplified cRNA was streptavidin-labeled, fragmented, and hybridized to Affymetrix 430–2.0 arrays (Affymetrix). Arrays were scanned with a Genechip Scanner 3000 (Affymetrix) running GCOS 1.1.1. software. Scanned data were exported to DCHIP software for

normalization. Raw microarray data were submitted to Gene Expression Commons (https://gexc.stanford.edu/) (21), where data normalization was computed against the Common Reference, a large collection (n = 11,939) of publicly available microarray data from the National Center for Biotechnology Information Gene Expression Omnibus. Metaanalysis of the Common Reference also provides the dynamic range of each probe set on the array. The probe set with the widest dynamic range was used for analysis. The Affymetrix Mouse Genome 430 2.0 Array includes 45,101 probe sets, of which 17,872 annotated genes are measurable. Heat maps representing fold change of gene expression were generated in Gene Expression Commons.

Hindlimb Irradiation. Eight-week-old C57BL/6 mice were placed in a radiation shield to expose only the hindlimbs. Mice received a single dose of 800 rad (8 Gy). Surgical fracture induction was done 12 h postirradiation.

Immunofluorescence Staining. BCSP-derived colonies were fixed with paraformaldehyde and labeled using a standard immunofluorescence staining protocol with monoclonal antibody to mouse collagen II (NeoMarkers) and monoclonal antibody to osteocalcin (Abcam). Alexa dye-conjugated secondary antibodies were purchased from Molecular Probes. After three rounds of washing with staining buffer, secondary antibodies were added. Samples were washed with PBS, cover-slipped, and imaged with a Leica DMI6000B epifluorescence-equipped inverted microscope.

FACS Analysis of Annexin V-Positive Cells. Quantification of Annexin V-positive BCSPs was conducted using an Annexin V: FITC Apoptosis detection kit II (BD). Cells were stained per the manufacturer's instructions and analyzed on a BD FACS ARIA II FACS Sorter.

Statistical Analysis. All statistical analysis was performed in GraphPad Prism (GraphPad Software). Data analysis was performed using one-way ANOVA and post hoc Tukey correction or Student's t test assuming two-tailed distribution and unequal variances. The use of an asterisk denotes statistical significance of $P < 0.05$ between the sample groups described. In graphs with more than two groups, statistical analysis describes the two groups connected by a bar line. All results are shown as mean ± SEM. All samples represent at least $n = 3$.

ACKNOWLEDGMENTS. We thank Shirley Kantoff and Terry Storm for laboratory management, Aaron McCarty and Felix Manuel for animal assistance, Patty Lovelace and Jennifer Ho for assistance in the Shared FACS Facility in the Lokey Stem Cell Institute, Timothy Doyle for assistance in the Small Animal Imaging Facility, and Gunsagar Gulati for technical assistance. We acknowledge the following support for this work: NIH Grants R01 DE021683-01, R21 DE02423001, 5 R01 DE019434, RC2 DE020771, and U01 HL099776 (to M.T.L.); NIH Grants U01HL099999, 5 R01 CA86065, and 5 R01 L058770 (to I.L.W.); a Siebel Fellowship from the Thomas and Stacey Siebel Foundation, Prostate Cancer Foundation Young Investigator Award (to C.K.F.C.); California Institute for Regenerative Medicine (CIRM) Grant TR1-01249, the Oak Foundation, the Hagey Laboratory for Pediatric Regenerative Medicine, the Gunn/Olivier Research Fund (to M.T.L.); Stanford University Transplant and Tissue Engineering Center of Excellence Fellowship (to A.M. and R.T.); a Plastic Surgery Foundation/Plastic Surgery Research Council Pilot Grant and an American Society of Maxillofacial Surgeons Research Grant (to R.T.).

1. Chan CK, et al. (2015) Identification and specification of the mouse skeletal stem cell. *Cell* 160(1-2):285–298.
2. Rinkevich Y, Lindau P, Ueno H, Longaker MT, Weissman IL (2011) Germ-layer and lineage-restricted stem/progenitors regenerate the mouse digit tip. *Nature* 476(7361): 409–413.
3. Rinkevich Y, et al. (2014) In vivo clonal analysis reveals lineage-restricted progenitor characteristics in mammalian kidney development, maintenance, and regeneration. *Cell Reports* 7(4):1270–1283.
4. Sherwood RI, et al. (2004) Isolation of adult mouse myogenic progenitors: Functional heterogeneity of cells within and engrafting skeletal muscle. *Cell* 119(4):543–554.
5. Slack JM (2000) Stem cells in epithelial tissues. *Science* 287(5457):1431–1433.
6. Spangrude GJ, Heimfeld S, Weissman IL (1988) Purification and characterization of mouse hematopoietic stem cells. *Science* 241(4861):58–62.
7. Beerman I, et al. (2010) Functionally distinct hematopoietic stem cells modulate hematopoietic lineage potential during aging by a mechanism of clonal expansion. *Proc Natl Acad Sci USA* 107(12):5465–5470.
8. Mendelson A, Frenette PS (2014) Hematopoietic stem cell niche maintenance during homeostasis and regeneration. *Nat Med* 20(8):833–846.
9. Pang WW, et al. (2011) Human bone marrow hematopoietic stem cells are increased in frequency and myeloid-biased with age. *Proc Natl Acad Sci USA* 108(50): 20012–20017.
10. Bryder D, Rossi DJ, Weissman IL (2006) Hematopoietic stem cells: The paradigmatic tissue-specific stem cell. *Am J Pathol* 169(2):338–346.
11. Chen L, et al.; BRIDGE Consortium (2014) Transcriptional diversity during lineage commitment of human blood progenitors. *Science* 345(6204):1251033.
12. Copley MR, Beer PA, Eaves CJ (2012) Hematopoietic stem cell heterogeneity takes center stage. *Cell Stem Cell* 10(6):690–697.
13. Morrison SJ, Weissman IL (1995) Heterogeneity of hematopoietic stem cells: Implications for clinical applications. *Proc Assoc Am Physicians* 107(2):187–194.
14. Chan CK, et al. (2013) Clonal precursor of bone, cartilage, and hematopoietic niche stromal cells. *Proc Natl Acad Sci USA* 110(31):12643–12648.
15. Park D, et al. (2012) Endogenous bone marrow MSCs are dynamic, fate-restricted participants in bone maintenance and regeneration. *Cell Stem Cell* 10(3):259–272.
16. Zhou BO, Yue R, Murphy MM, Peyer JG, Morrison SJ (2014) Leptin-receptor-expressing mesenchymal stromal cells represent the main source of bone formed by adult bone marrow. *Cell Stem Cell* 15(2):154–168.
17. Ito K, Perren SM (2007) Biology and biomechanics in bone healing. *AO Principles of Fracture Management*, eds Rüedi TP, Buckley RE, Moran CG (AO Publishing, Switzerland) 2nd Ed, Vol 1, pp 8–31.
18. Eastaugh-Waring SJ, Joslin CC, Hardy JR, Cunningham JL (2009) Quantification of fracture healing from radiographs using the maximum callus index. *Clin Orthop Relat Res* 467(8):1986–1991.
19. Mitchell MJ, Logan PM (1998) Radiation-induced changes in bone. *Radiographics* 18(5):1125–1136.
20. Chan CK, et al. (2009) Endochondral ossification is required for haematopoietic stem-cell niche formation. *Nature* 457(7228):490–494.
21. Seita J, et al. (2012) Gene Expression Commons: An open platform for absolute gene expression profiling. *PLoS One* 7(7):e40321.
22. Musumeci G, et al. (2013) Post-traumatic caspase-3 expression in the adjacent areas of growth plate injury site: A morphological study. *Int J Mol Sci* 14(8):15767–15784.
23. Wang H, et al. (2014) CARD11 blockade suppresses murine collagen-induced arthritis via inhibiting CARD11/Bcl10 assembly and T helper type 17 response. *Clin Exp Immunol* 176(2):238–245.
24. Adhami MD, et al. (2015) Loss of runx2 in committed osteoblasts impairs postnatal skeletogenesis. *J Bone Miner Res* 30(1):71–82.
25. Leung VY, et al. (2011) SOX9 governs differentiation stage-specific gene expression in growth plate chondrocytes via direct concomitant transactivation and repression. *PLoS Genet* 7(11):e1002356.
26. Wang Q, Huang C, Xue M, Zhang X (2011) Expression of endogenous BMP-2 in periosteal progenitor cells is essential for bone healing. *Bone* 48(3):524–532.
27. Anderson RM, Lawrence AR, Stottmann RW, Bachiller D, Klingensmith J (2002) Chordin and noggin promote organizing centers of forebrain development in the mouse. *Development* 129(21):4975–4987.
28. Suzuki D, et al. (2012) BMP2 differentially regulates the expression of Gremlin1 and Gremlin2, the negative regulators of BMP function, during osteoblast differentiation. *Calcif Tissue Int* 91(1):88–96.
29. Bijakowski C, et al. (2012) Sizzled is unique among secreted frizzled-related proteins for its ability to specifically inhibit bone morphogenetic protein-1 (BMP-1)/tolloid-like proteinases. *J Biol Chem* 287(40):33581–33593.
30. Cho SW, et al. (2009) Wnt inhibitory factor (WIF)-1 inhibits osteoblastic differentiation in mouse embryonic mesenchymal cells. *Bone* 44(6):1069–1077.
31. Jin H, et al. (2015) Anti-DKK1 antibody promotes bone fracture healing through activation of β-catenin signaling. *Bone* 71:63–75.
32. Amanai K, Jiang J (2001) Distinct roles of Central missing and Dispatched in sending the Hedgehog signal. *Development* 128(24):5119–5127.
33. Amano K, Densmore M, Nishimura R, Lanske B (2014) Indian hedgehog signaling regulates transcription and expression of collagen type X via Runx2/Smads interactions. *J Biol Chem* 289(36):24898–24910.
34. Yang WJ, et al. (2005) Dicer is required for embryonic angiogenesis during mouse development. *J Biol Chem* 280(10):9330–9335.
35. Galloway JL, Delgado I, Ros MA, Tabin CJ (2009) A reevaluation of X-irradiation-induced phocomelia and proximodistal limb patterning. *Nature* 460(7253):400–404.
36. Notta F, et al. (2011) Isolation of single human hematopoietic stem cells capable of long-term multilineage engraftment. *Science* 333(6039):218–221.
37. Wagers AJ, Allsopp RC, Weissman IL (2002) Changes in integrin expression are associated with altered homing properties of Lin(-/lo)Thy1.1(lo)Sca-1(+)c-kit(+) hematopoietic stem cells following mobilization by cyclophosphamide/granulocyte colony-stimulating factor. *Exp Hematol* 30(2):176–185.
38. Chung MT, et al. (2013) Isolation of human adipose-derived stromal cells using laser-assisted liposuction and their therapeutic potential in regenerative medicine. *Stem Cells Transl Med* 2(10):808–817.
39. Garvey et al. (1986) Improved Movat pentachrome stain. *Stain technology* 61(1): 60–62.